



Establishing Structure/Property Relationships in Atomically Dispersed Co-Fe Dual Sites M-N_x Catalysts on Microporous Carbon for Oxygen Reduction Reaction

Journal:	<i>Journal of Materials Chemistry A</i>
Manuscript ID	TA-ART-04-2021-002925.R1
Article Type:	Paper
Date Submitted by the Author:	09-May-2021
Complete List of Authors:	Wang, Kai; South China University of Technology, Liu, Jiapeng; The Hong Kong University of Science and Technology, Tang, Zhenghua; South China University of Technology, School of Environment and Energy Li, Liqui; South China University of Technology, Wang, Zheng; Peking University Shenzhen Graduate School, Guangdong Key Lab of Nano-Micro Material Research, School of Chemical Biology and Biotechnology; Peking University Shenzhen Graduate School Zubair, Muhammad; University of New South Wales Faculty of Engineering Ciucci, Francesco; Hong Kong University of Science and Technology, MAE & CBME Thomsen, Lars; Australian Synchrotron Wright, Joshua; Univ of Maine, Bedford, Nicholas; University of New South Wales Faculty of Engineering,

ARTICLE

Establishing Structure/Property Relationships in Atomically Dispersed Co-Fe Dual Sites M-N_x Catalysts on Microporous Carbon for Oxygen Reduction Reaction

Received 00th January 20xx,
Accepted 00th January 20xx

DOI: 10.1039/x0xx00000x

Kai Wang,^{a,#} Jiapeng Liu,^{b,#} Zhenghua Tang,^{a,c,*} Ligui Li,^a Zheng Wang,^b Muhammad Zubair,^d Francesco Ciucci,^{b,e,*} Lars Thomsen,^f Joshua Wright,^g and Nicholas M. Bedford^{d,*}

Coupled metal-nitrogen-carbon (M-N_x-C) materials show great promise as platinum-group-metal (PGM) free catalysts for oxygen reduction reaction (ORR). Herein, we report a facile strategy to construct atomically dispersed Co, Fe dual sites enriched onto the surface of nitrogen doped microporous carbon (NC) as an efficient electrocatalyst for ORR. Synchrotron X-ray techniques indicate that Co and Fe atoms are strongly correlated while further revealing longer-range lattice structure of NC is highly tunable. Density functional theory calculations reveal Co-Fe dimers are incorporated in the slightly disordered NC substrate, providing a lower adsorption free energy for O₂. The as-prepared CoFe-NC catalyst exhibited excellent ORR activities, with a CoFe-NC based zinc air battery exhibited a power density of 115 mW cm⁻² and a specific capacity of 791 mA h g⁻¹. This work showcases a straightforward methodology for creating atomically dispersed catalyst and illustrates the importance of understanding how dual metal sites impact the electrocatalytic activity.

Introduction

To mitigate the global energy reliance on fossil fuels and to help alleviate the worldwide environmental pollution issues, it is imperative to develop renewable and sustainable energy devices such as proton exchange membrane fuel cells (PEMFCs) and metal air batteries.^{1, 2} The oxygen reduction reaction (ORR) is a key process which significantly influences the energy conversion efficiency of the aforementioned devices, but is impeded partially by the reduction of strong O=O bonds (498 kJ mol⁻¹), resulting in sluggish reaction kinetics that necessitates electrocatalytic materials.³ Platinum-based catalysts, especially Pt/C, have been the benchmark catalyst for desirable ORR reactivity, yet are commercialized prohibitive due to the high cost and scarcity of Pt.⁴ Additionally, Pt-based catalysts suffer from other ineluctable problems, such as poor durability for

prolonged operation, susceptible to methanol crossover and so on.^{5, 6}

In an effort to move away from Pt and similar problematic Pt group metal (PGM) catalysts, the emergence of first-row transition metal nitrogen-doped porous carbon (M-N_x-C) materials have gained serious attention as promising alternatives for ORR. Previous reports have demonstrated that M-N_x-C catalyst show excellent catalytic performance, which is coupled with inherently low cost and potential ability to tune the chemistry/structure of well-defined active sites have led to surge in research activities.⁷⁻⁹ In regards to ORR, the bonding energies of M-N_x sites with oxygen molecules and oxygenated intermediates are dependent on the nature of the transition metal and local structure, which results in significantly different activities and stabilities.¹⁰ With high utilization of metal centers and strong anchoring interaction between the nitrogen and metal atoms, the atomically dispersed M-N_x-C catalysts (also often called single-atom catalysts, SACs) have demonstrated excellent activity and robust stability, even superior to that of the state-of-the-art Pt/C catalyst for ORR.^{11, 12} For example, Wan *et al.* fabricated a concave-shaped Fe-N-C single atom catalyst with enhanced external surface area and dense Fe-N₄ moieties, which demonstrated an extremely high PEMFC activity that surpassed 2018 US DOE targets.¹³ Other atomically dispersed transition metal based M-N_x-C catalysts including Co-N_x-C,¹⁴ Mn-N_x-C,¹⁵ Ni-N_x-C,¹⁶ Zn-N_x-C,¹⁷ Cu-N_x-C,¹⁸ Ir-N_x-C,¹⁹ Cr-N_x-C,²⁰ and Ru-N_x-C²¹ have also been explored for ORR electrocatalysis. The use of dual transition metal active sites in M-N_x-C are increasingly studied as well, mainly due to the synergistic effects between two metallic atoms that result in charge redistribution and d-band center shift.^{22, 23} For example, Wu and colleagues constructed atomically dispersed Co-Fe dual

^a Guangzhou Key Laboratory for Surface Chemistry of Energy Materials and New Energy Research Institute, School of Environment and Energy, South China University of Technology Guangzhou Higher Education Mega Center, Guangzhou, Guangdong 510006, China. E-mail: zhht@scut.edu.cn

^b Department of Mechanical and Aerospace Engineering, The Hong Kong University of Science and Technology, Hong Kong, 999077, SAR, China. E-mail: francesco.ciucci@ust.hk

^c Key Laboratory of Fuel Cell Technology of Guangdong Province, School of Chemistry and Chemical Engineering, South China University of Technology, Guangzhou, 510640, China.

^d School of Chemical Engineering University of New South Wales Sydney, New South Wales, 2052, Australia.

^e Department of Chemical and Biological Engineering, The Hong Kong University of Science and Technology, Hong Kong, 999077, SAR, China.

^f Australian Synchrotron, ANSTO, Clayton, Victoria, 3168, Australia.

^g Department of Physics, Illinois Institute of Technology, Chicago, Illinois, 60616, United States. E-mail: n.bedford@unsw.edu.au

These authors contributed equally to this work.

Electronic Supplementary Information (ESI) available: See DOI: 10.1039/x0xx00000x

sites embedded on N-doped porous carbon, which had an onset potential of 1.06 V and a half wave potential of 0.86 V in acidic electrolyte.²⁴ The same group also reported a novel electrocatalyst with Co-Fe dual sites embedded in N-doped carbon nanotubes, which showed an onset potential of 1.15 V and a half wave potential of 0.954 V in alkaline solution.²⁵ Density functional theory (DFT) calculation results revealed that the Fe, Co dual sites could reduce the cleavage barrier energy of O=O bond to achieve high activity and preferential selectivity of the 4-electron transfer pathway in ORR.^{24, 25} In addition, Xiao et. al discovered that, the anchoring of OH⁻ on the Co-Fe dual-atom centered FeCoN₅ site could enable an optimal e_g-orbital energy level for Fe and a favorable geometry configuration for a desirable O=O bridge adsorption which significantly boosted the ORR performance.²⁶ Furthermore, other studies on binary M-N_x-C systems also show that, bimetallic architecture can elongate the O-O bond length to facilitate the bond cleavage, and the adjacent two-metals can modulate the electronic interaction to promote the ORR activity eventually.^{27, 28} Herein, we report a facile strategy to synthesize atomically dispersed CoFe-N_x-C catalysts, using inexpensive phenol formaldehyde resin (PFR) spheres and NH₄Cl as co-anchors to maximize the reactive surface sites. Metal ions are adsorbed into PFR spheres and initially anchored by surface N atoms and NH₄Cl. This complex is then pyrolyzed to form atomically dispersed CoFe-NC, in which NH₄Cl plays an additional role of forming pores in the carbon matrix. As a result, the CoFe-N_x sites are uniformly distributed on the surface of the nitrogen doped microporous carbon (NC) and the inner wall of the pores, which ensures the accessibility to the active sites. Atomically dispersed CoFe-N_x sites were characterized with atomic resolution high-angle annular dark-field scanning transmission electron microscopy (HAADF-STEM), X-ray absorption spectroscopy (XAS), and atomic pair distribution function (PDF) analysis. XAS studies show that the coordination motif of nitrogen with Co, Fe resembles a N₃Co-FeN₃, with the Co atoms likely being responsible for the formation of this catalytic motif. The PDF analysis further indicates longer range structural organization of Co and Fe atoms while modulating the overall structural coherence within the disordered carbon. DFT calculations reveal that N₃Co-FeN₃ active motif acts as an excellent active center toward ORR on the slightly disordered carbon substrate. The as-prepared CoFe-NC catalyst exhibited a superior ORR performance to the Pt/C catalyst in alkaline media, thanks to the appropriate adsorption energies of the oxygenated species and strong molecular orbital interaction from the atomic Co-Fe dimers as revealed by the computational models. As air cathode, CoFe-NC also demonstrated outperformed properties than Pt/C in our zinc air battery experiments. While desirable properties were obtained using Co and Fe dual sites catalysts, we envision this synthetic route and subsequent characterization strategies are readily adaptable to a range of atomically dispersed M-N_x-C catalysts to enhance reactivities in a series of possible reactions.

Experimental

Materials

Cobalt chloride hexahydrate (CoCl₂·6H₂O, AR) and ferric chloride hexahydrate (AR, FeCl₃·6H₂O), 4-aminophenol (AR) and ammonium chloride (AR, NH₄Cl) were purchased from Sinopharm Chemical Reagent Co., Ltd (Shanghai, China). Formaldehyde (AR, 37%), pluronic F-127 (AR), ammonium hydroxide (AR, 28%), ethanol (AR) and potassium hydroxide (95% KOH) were acquired from Energy Chemicals (Shanghai, China). Nitric acid (AR, 65% HNO₃) and perchloric acid (AR, 70% HClO₄) were procured from Guangzhou Chemical Reagent Factory (Guangzhou, China). Commercial 20% Pt/C was obtained from Alfa Aesar. Nafion was acquired from Dupont (USA). All aqueous solutions were prepared using deionized (DI) water with a resistivity of 18.3 MΩ·cm.

Synthesis of phenol formaldehyde resin (PFR) nanospheres

1.5 g F-127 was first dissolved in 20 mL DI H₂O, then added 4-aminophenol of 0.5 g to above solution, ultrasonically dispersed mixed solution for 5 min. Secondly, 0.35 mL of formaldehyde and 0.3 mL NH₃·H₂O were diluted by 10 mL DI H₂O and added into above mixed solution at room temperature, then heated to 80 °C and kept stirring for 18 h. Finally, the sample was washed with DI H₂O and dried at 35 °C for 12 h in the vacuum oven. Among them, NH₃·H₂O was used as a catalyst for phenolic resin condensation. The final sample was marked as PFR.

Preparation of atomically dispersed CoFe-NC, Co-NC, and Fe-NC

The typical preparation process of the CoFe-NC as follows; 0.5 mmol CoCl₂·6H₂O and 0.5 mmol FeCl₃·6H₂O were dissolved in 10 mL DI H₂O, then 100 mg PFR was added into mixed solution and ultrasonic dispersion for 5 min. To promote the Co²⁺, Fe³⁺ ions can be uniformly and fully adsorbed by the PFR, the mixed solution needs to be slowly stirred at room temperature for 4 h. Subsequently, freezing-dried above solution at -50 °C for 12 h, the sample was marked to CoFe/PFR. Above CoFe/PFR and 4.0 g NH₄Cl were ground in an agate mortar for 10 min, and then carbonized at 900 °C for 2 h with the heating rate of 2 °C min⁻¹. Finally, etching those CoFe particles that did not form a stable structure with NC by 2 M HNO₃, the sample was marked to CoFe-NC (the same sample of CoFe-NC-900 in Fig. S1, and CoFe-35 in Fig. S2, 35 is the initial total metal loading percentage of Co and Fe). The samples with carbonization temperature at 800 °C and 1000 °C were also prepared (CoFe-NC-800 and CoFe-NC-1000 in Fig. S1). In addition, the method for preparing CoFe-25, CoFe-30, CoFe-40 and CoFe-45 (Fig. S2) is similar with that of CoFe-NC (CoFe-35), besides the amount of CoCl₂·6H₂O is 0.3 mmol, 0.4 mmol, 0.6 mmol and 0.7 mmol, FeCl₃·6H₂O is 0.3 mmol, 0.4 mmol, 0.6 mmol and 0.7 mmol for CoFe-25, CoFe-30, CoFe-40 and CoFe-45, respectively. Set the molar amount of total metal ions of 1.0 mmol and then adjusting the ratio of Co-to-Fe as 1: 3 and 3: 1, Co₃Fe-NC and CoFe₃-NC (Fig. S3) can be synthesized according to the preparation method of CoFe-NC (Co: Fe= 1: 1). The method for preparing Co-NC and Fe-NC are the same as that of the CoFe-NC, the difference is that for Co-NC, the amount of CoCl₂·6H₂O was increased to 1 mmol and without FeCl₃·6H₂O, for the Fe-NC is that FeCl₃·6H₂O was increased to 1 mmol and without CoCl₂·6H₂O.

Preparation of OMC, NC, and atomically dispersed CoFe-C

The OMC was prepared by carbonizing the PFR at 900 °C with the heating rate of 2 °C min⁻¹ for 2 h. The NC was prepared by carbonizing the mixture of PFR (100 mg) and NH₄Cl (4.0 g) at 900 °C with the heating rate of 2 °C min⁻¹ for 2 h. The CoFe-C was synthesized according to CoFe-NC method, the only difference is direct carbonization without NH₄Cl after freezing-dried.

Details on electrochemical measurements, characterization, and simulation methods can be found in Electronic Supplementary Information (ESI).

Results and discussion

Synthesis, SEM, and TEM characterization

CoFe-NC (Co-Fe dual sites onto the nitrogen doped microporous carbon) was first synthesized by following the route in Fig. 1a (see Supporting Information for details). Briefly, the phenol formaldehyde resin (PFR) spheres were first prepared through polycondensation of 4-aminophenol and formaldehyde with F-127 that served as the surfactant to control the size and as structural direct agent for forming PFR.²⁹ Subsequently, Co²⁺ and Fe³⁺ ions were absorbed into the pores of the PFR by van der Waals force, and initially anchored with nitrogen by coordination (termed as CoFe/PFR). CoFe/PFR and NH₄Cl were

in Fig. 1b, PFR holds a well-defined pore structure with the diameter of the spheres about 134 ± 27 nm. Such carbon skeleton was mostly well preserved in the final product of CoFe-NC upon 900 °C calcination, as depicted in Fig. 1c. However, there are some amorphous carbon layers formed onto the surface of carbon spheres. N₂ adsorption-desorption isotherm of CoFe-NC can be found in Fig. 1d, where CoFe-NC possessed a large specific surface area of ~830 m² g⁻¹, total pore volume of ~3.49 cm³ g⁻¹ and uniform micropores with the pore diameter of ~1.86 nm. Transmission electron microscopy (TEM) was performed to investigate bulk or nanoscale metals/metal oxides in CoFe-NC. As shown in Fig. 1e, f and g, nanoscale CoFe particles were not detected in CoFe-NC. Moreover, X-ray diffraction (XRD) patterns (Fig. 1h) also do not show any diffraction peak of Co, Fe or CoFe alloyed particles nor their associated metal oxides, only two broad peaks at 2θ = 24.3° and 43.2° associated with the microporous C.

It is important to note that F-127 is critical as the morphology control agent for forming the ordered pore structure of PFR. In the presence of F-127, formaldehyde and 4-aminophenol formed micelles that then solidify to yield the resols/F-127 composite by cross-linking between 4-aminophenol and formaldehyde.²⁹ When F127 is partially removed with excess ethanol and deionized water, the ordered pore structure will be

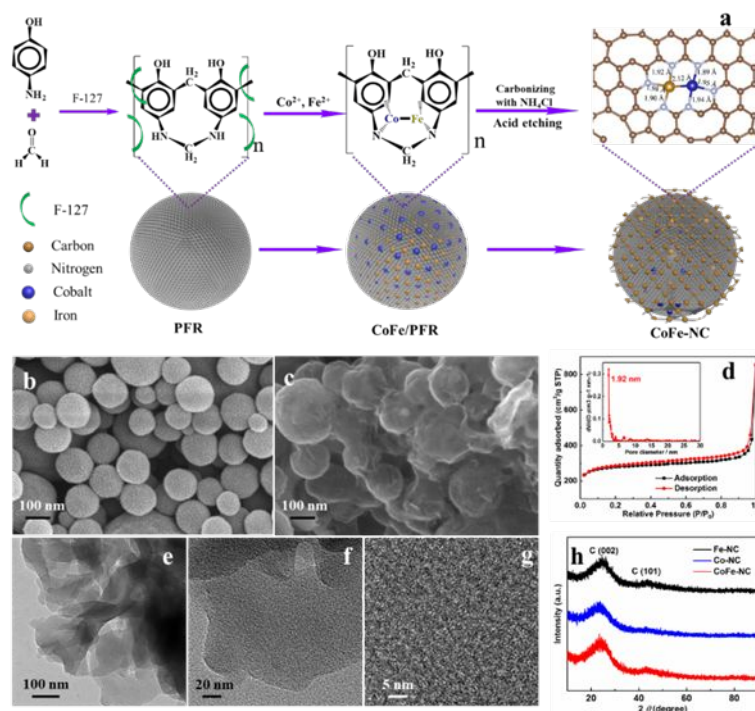


Fig. 1. (a) Schematic illustration for synthesizing CoFe-NC; (b) and (c) are the typical SEM images of PFR and CoFe-NC, respectively; (d) The N₂ adsorption-desorption isotherms (inset is the pore size distribution) of CoFe-NC; (e-g) The typical TEM images of CoFe-NC with different magnifications; (h) The XRD patterns of Fe-NC, Co-NC, and CoFe-NC.

then mixed by grinding and carbonized under Ar atmosphere, followed by chemical etching in nitric acid to remove the inactive and unstable species. The catalyst (denoted as CoFe-NC) was then washed and dried for further catalytic testing and characterization.

The morphological change during each step of the synthesis was monitored using scanning electron microscopy (SEM). As shown

formed on the surface of PFR by the accumulation and rearrangement of small spherical micelles.³⁰ Previously it has been demonstrated that F-127 held strong confinement effects which suppressed the agglomeration of Co atomic sites during the thermal activation in forming Co-N₄.³¹ Here, we are using F-127 to suppress metal agglomeration. Moreover, the introduction of NH₄Cl in the calcination process also plays a

crucial role in the formation of the CoFe-NC. A typical SEM image of the OMC (PFR pyrolyzed at 900 °C without NH₄Cl), NC (PFR pyrolyzed at 900 °C with NH₄Cl), and CoFe-C (CoFe/PFR pyrolyzed at 900 °C without NH₄Cl) samples can be found in **Fig. S4**. Without adding NH₄Cl, “naked” carbon spheres were obtained (OMC in **Fig. S4a** and CoFe-C in **Fig. S4c**), but with the presence of NH₄Cl, amorphous carbon layers were formed onto the surface of carbon spheres (NC in **Fig. S4b**). **Fig. S4d** presents the N₂ adsorption-desorption isotherms of OMC-900, NC, and CoFe-C. The specific surface area, total pore volume and the pore diameter of OMC-900, NC, CoFe-C, and CoFe-NC are summarized in **Table S1**. Compared with OMC-900 and CoFe-C, NC and CoFe-NC possessed higher specific surface areas and larger pore volumes, respectively. Such phenomenon indicates that the introduction of NH₄Cl can etch the carbon matrix during pyrolysis to form micropore which leads to the enhanced specific surface area. Therefore, NH₄Cl can not only provide additional nitrogen source to anchor the Co, Fe atoms, but also was able to promote the formation of amorphous carbon layers on the surface of CoFe-NC, and enhance the surface area and the pore volume as well. As a note, the abundant uniform micropores and large specific surface area in CoFe-NC is expected to maximize the density of the active sites and promote the mass transport for electrocatalytic reactions.³²

HAADF-STEM, XANES, XEAFS analysis and PDF modeling

dispersed on the C support. The inset highlights that a majority of metal atoms in the HAADF-STEM are coupled together, indicating the formation of Co-Fe dual sites. This result was further verified by using electron energy-loss spectroscopy (EELS). As shown in **Fig. S5**, when the electron beam was sputtered on the white rectangle area in **Fig. 2a**, both Fe and Co are present in the spectrum, indicating that the Fe, Co atoms coexist in the CoFe-NC catalyst. Note that, a small amount of isolated Co or Fe sites were also observed in the HAADF-STEM image. The coordination between Co, Fe, and N atoms can be examined by HAADF-STEM measurements in conjunction with EELS mapping. The corresponding EELS mapping (**Fig. 2b**) further shows that the Co, Fe atoms are dispersed by single atom and diatoms in CoFe-NC, rather than clusters or nanoparticles. In addition, **Fig. S6a** and **b** reveal that Co and Fe single atoms are atomically dispersed in the Co-NC and Fe-NC samples, respectively, suggesting that this method can be applied to synthesize atomically dispersed monometallic catalysts as well. The surface composition and electronic structure of the CoFe-NC sample were then probed by XPS measurements. The XPS survey scan spectra show the coexistence of C (92.03 at%), N (6.74 at%), Co (0.73 at%), and Fe (0.50 at%) species in CoFe-NC (**Fig. S7**). The corresponding weight percentages of the Co, Fe elements in CoFe-NC estimated from XPS are 3.39% and 2.15%, and to further

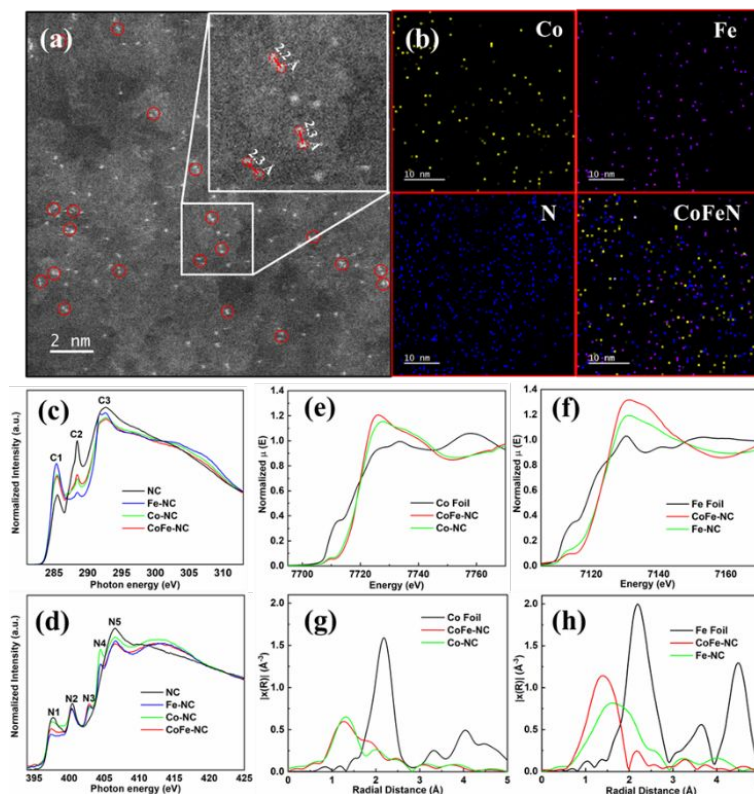


Fig. 2 (a) Atomic-resolution high-angle annular dark-field (AR-HAADF) scanning TEM image of CoFe-NC; (b) Corresponding EELS mapping of Co, Fe, N, and the composite image; (c) C K-edge and (d) N K-edge NEXAFS spectra of NC, Co-NC, Fe-NC and CoFe-NC; (e) Co K-edge and (f) Fe K-edge XANES spectra, (g) Co K-edge and (h) Fe K-edge EXAFS spectra of the Co-NC, Fe-NC, and CoFe-NC.

To further probe the atomic dispersity in CoFe-NC, high angle annular dark field scanning transmission electron microscopy (HAADF-STEM) was performed (**Fig. 2a**). A large number of Co and Fe atoms are prevalent as bright spots and are well

confirm such values, inductively coupled plasmon-atomic emission spectroscopy (ICP-AES) test was conducted, and the results are summarized in **Table S2**. It is worth noting that, the actual Co and Fe contents in Co-NC, Fe-NC, and CoFe-NC

determined from ICP-AES are lower than the values from XPS. This is mainly due to that XPS is a surface sensitive detection technique, and in the above samples, the metal atoms are enriched on the surface of carbon substrate, resulting in the contents of metal atoms detected by XPS being higher than that from ICP-AES.

The high resolution XPS N 1s spectra of CoFe-NC along with OMC-900 and NC are illustrated in **Fig. S8a**. For all the samples, four sub-peaks corresponding to pyridinic N, pyrrolic N, graphitic N, and oxidized N can be deconvoluted.³³ Of particular note, the pyridinic N in OMC-900 and NC possessed the identical binding energy (398.1 eV), while this peak in CoFe-NC shifts to 398.5 eV. The peak position of the other N species in CoFe-NC are the same as OMC-900 and NC, indicating that Co, Fe atoms are bonded by pyridinic N to form the CoFe-N moieties. **Fig. S8b** compiles the concentration of the four N species for the samples. This indicates that the concentration of pyridinic N in CoFe-NC (2.42 at%) is higher than that in OMC-900 (0.82 at%) and NC (1.63 at%), suggesting CoFe-NC contains a large number of edge structure, which could generate plentiful edge nitrogen contained CoFe-N_x moieties. Moreover, the binding energies of the Co 2p (**Fig. S9a**) and Fe 2p (**Fig. S9b**) electrons in CoFe-NC slightly shift to higher values compared to Co-NC and Fe-NC, indicating that they have higher oxidation state.

To further probe the electronic structure of the catalysts, XAS measurements were performed at the K-edge of each element in our catalysts. Near edge X-ray absorption fine structure (NEXAFS) measurements at the C K-edge (**Fig. 2c**) exhibit peaks labeled C1 and C3 at 285.3 and 292.5 eV which are mainly derived from aromatic C-C π^* and C-C σ^* transitions, respectively.³⁴ Compared to NC, Co-NC, Fe-NC, and CoFe-NC exhibited an obvious intensity increase of C1 peak and decrease of C3 peak, suggesting an increasing of π -network electron density toward the catalysts atoms.³⁴ Noticeably, a sharp peak at 288.5 eV (C2) was detected for NC, Co-NC, Fe-NC, and CoFe-NC, which is attributed to C-N bonding.³⁵ By contrast, the C2 peak intensity of NC was stronger than that of Co-NC, Fe-NC, and CoFe-NC catalyst, likely due to partial removal of C-N-C moieties with the inclusion of M-N_x-C sites.³⁶ N K-edge NEXAFS spectra (**Fig. 2d**) exhibited five sharp peaks labeled N1, N2, N3, N4 and N5, which can be assigned to pyridinic N π^* , graphitic N, N-N, N-O and C=N σ^* transitions, respectively.³⁷ Compared to NC, the intensity of the N1, N2, and N5 peaks decrease in Co-NC, Fe-NC, and CoFe-NC, while N3 and N4 peaks show a marked increase in intensity, implying the removal of C=N bonds and formation of metal-N coordination after pyrolysis.³⁸

The electronic structure and the local coordination environment of the metal atoms within CoFe-NC, Co-NC, and Fe-NC was then examined at the K-edges of the respective metals. **Fig. 2e** shows the Co K-edge XANES spectra of CoFe-NC and Co-NC compared with a Co foil reference. It can be noted that CoFe-NC and Co-NC possessed higher intensity white lines compared to Co foil, indicating non-metallic Co exist in the atomically dispersed samples.³⁹ In addition, the white line intensity of CoFe-NC is slightly higher than that of Co-NC, likely due to Co-Fe intermetallic electron transfer between the Co and Fe atoms in the coupled metal system and/or through

interactions with neighboring N atoms. Similarly, the Fe K-edge XANES of CoFe-NC and Fe-NC indicate that non-metallic iron or bulk oxidized Fe is obtained, exhibiting similar features of previously reported atomically dispersed Fe (**Fig. 2f**).⁴⁰ The white line intensity of the Co-Fe system again is higher overall while coupled with a decrease in the pre-edge feature, indicating that the Co-Fe due site catalyst is losing electron density when paired together. Bader charge analysis of the different catalyst configurations (**Table S3**) indicate an increased removal of charge from both the Fe and Co atoms in the dual site CoFe as compared to single metal sites. This decrease in charge at the metal atoms is coupled with an increase in electron accumulation on the N atoms, is consistent with our XANES findings. Additional discussion on the DFT calculations of these materials can be found below.

The Fourier-transformed (FT) k^2 -extended X-ray absorption fine structure (EXAFS) spectra for Fe and Co K-edges are shown in **Fig. 2g** and **Fig. 2h** along with reference metal foils (not corrected for phase shift). Corresponding k^2 -space data is provided in **Fig. S10**. At the Co K-edge, the dominant peaks are positioned at 1.32 Å and 1.26 Å for the Co-NC and CoFe-NC, respectively, and arise from the local Co-N coordination environment. Lower magnitude features at higher radial distance can be observed in both Co-NC and CoFe-NC which likely reflect the nearest neighbor distances (NNDs) to carbon-based coordination spheres around the Co atoms and binary metallic pairs in CoFe-NC. The Fe K-edge EXAFS provides similar information, with Fe-N coordination distances positioned at 1.56 Å and 1.38 Å for Fe-NC and CoFe-NC, respectively. The main EXAFS feature in Fe-NC is notably broader with a likely additional EXAFS contribution at 1.87 Å. Note that, from both metal EXAFS data, the binary metal system produces a shorter M-N NND, indicating the secondary metal is directly influencing the immediate coordination environment.

The EXAFS data was then modeled using backscattering contributions from known metal coordination complexes as described in the experimental section. The modelling results are summarized in **Table S4** and shown in **Fig. S11**. For Co-NC, a Co-N coordination number (CN) of 2.74 ± 0.46 was calculated, indicating a near Co-N₃ local coordination environment. An average Co-N NND of 1.93 ± 0.01 Å was obtained through modeling, which is consistent with the similarly reported catalytic sites.³⁹ To obtain a satisfactory EXAFS fit, 2nd and 3rd coordination spheres with C were modeled with respective CNs of 4.66 ± 1.73 and 5.04 ± 2.16 at distances of 2.63 ± 0.04 Å and 2.84 ± 0.04 Å. Fe-NC was modelled in a similar fashion and exhibits higher CNs for Fe-N and the first Fe-C coordination sphere. The results are summarized in **Table S5** and shown in **Fig. S11**. This outcome indicates that the presence of metal species influences the formation and structure of the catalyst, which could have implications in overall catalytic activity and catalysts design.

The binary CoFe-NC was also modeled using both information from the Fe and Co K-edges simultaneously (**Table S4** and **S5**). As shown in **Fig. S11**, the CNs corresponding to the metal-metal is found to be 1.02 ± 0.21 at an NND of 2.07 ± 0.02 Å. This result indicates that the majority of metal atoms form dimers during

synthesis, albeit with a moderate uncertainty that arises from the low amounts of non-dimerized metals. Corresponding Fe-N and Co-N CNs are similar, with an Fe-N CN of 3.24 ± 0.48 and a Co-N CN of 3.23 ± 0.46 at respective NNDs of 1.94 ± 0.01 Å and 1.85 ± 0.01 Å. The positions of the M-N bonds are similar in the binary catalyst as compared to their mono-metallic counterparts with a MN_3 -type geometry. The C lattice in NC is significantly disordered here as well, as low Co-C CNs are again obtained while this distance could not be modeled from the Fe K-edge. Overall, these results showcase the largely coupled binary catalyst through the templating methodology used here provides a means to create unique and tunable catalytic active

XRD/PDF analysis is an ideal structural characterization method for nanoscale materials,⁴⁴ as atomic pair distances > 30 Å can be determined through diffraction experiments without the need for long range order.⁴⁵ If an appropriate background is available, a differential PDF (dPDF) can be obtained to probe the structure of minority species within a large lattice.⁴⁶ Here, we use dPDF to better understand the influence of catalyst structure by subtracting out all non-metal atomic pairs using the NC PDF.

As shown in **Fig. 3a**, longer range ordering resulting from metal-derived atomic pairs differs across all three atomically dispersed materials. Both $Co-N_x$ and $CoFe-N_x$ exhibit a feature at 1.92 Å, which is arising from M-N and agrees with our EXAFS results.

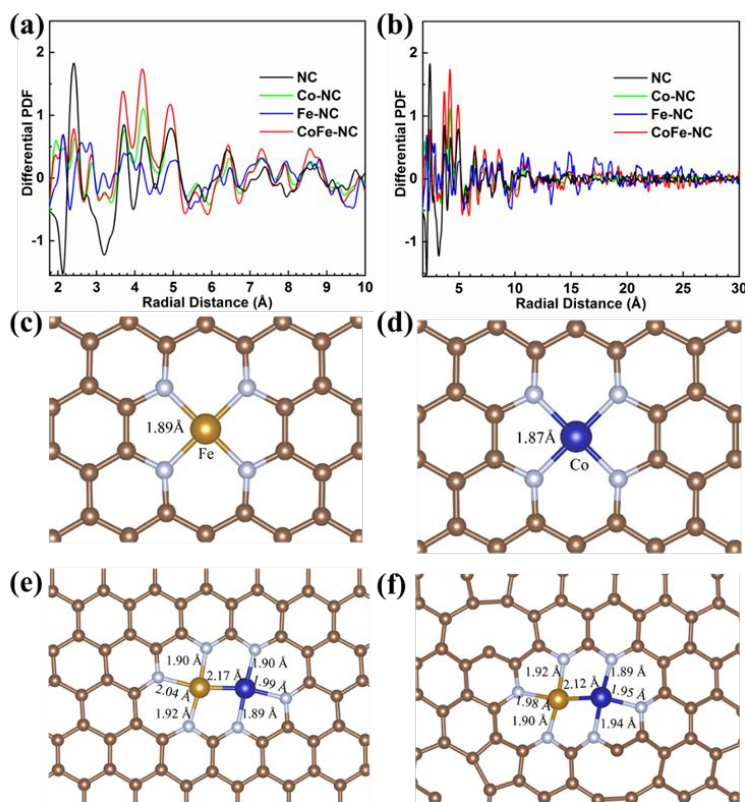


Fig. 3. (a) Differential atomic pair distribution function (dPDF) analysis at 10 Å and 30 Å (b) of the Co-NC, Fe-NC and CoFe-NC samples. The top view of the optimized structures for (c) single atom Fe on the NC substrate in the Fe-NC sample, (d) single atom Co on the NC substrate in the Co-NC sample. (e) and (f) show the Co-Fe dimer atoms on (e) the highly ordered NC substrate and (f) the slightly disordered NC substrate. The C, N atoms are in brown and cyan, respectively, only the Fe and Co atoms in (c) and (d) are labelled for clarity. The distance of Fe-N and Co-N are labelled near the bond.

sites.

While EXAFS can provide localized structural information around the desired element, longer-range structure is difficult to ascertain. This missing structural information may be critically important, as the dispersion of metal atoms and its associated effect on the matrix structure likely plays a major role determining the material's catalytic properties. Given the known influences of structural defects on the electronic structure of nanoscale carbon materials,⁴¹⁻⁴³ understanding the structure of both the local catalyst environment and the host may prove useful in understanding the catalytic properties of $M-N_x-C$ materials. To this end, we probed the atomically dispersed catalysts using high-energy X-ray diffraction (HE-XRD) coupled to atomic pair distribution function (PDF) analysis. HE-

The first dPDF peak in $Fe-N_x$ occurs at 2.14 Å, which is also present in the $CoFe-N_x$. This feature again agrees well with the Fe-N NNDs from EXAFS modeling of the Fe K-edge for $Fe-N_x$ and Co-Fe in $CoFe-N_x$. At longer atomic-pair distances, structural changes can be clearly observed by the dPDF. Most notably are the dPDF peaks found within $Fe-N_x$ from ~ 2.5 -3.5 Å, which are pronouncedly different from those observed in $Co-N_x$ and $CoFe-N_x$. This finding suggests that interactions within the carbon lattice between Co and Fe are quite different, and that Co has a stronger influence in forming the eventual final structure of the catalysts. In addition, $Co-N_x$ and $CoFe-N_x$ exhibit peaks that align more closely with the NC, which is essentially a graphite-like lattice, while $Fe-N_x$ tends to shift away from this lattice. Observations from longer range dPDFs (**Fig. 3b**) show relative

increased overall atomic order in Fe-N_x, further showcasing the differences of the NC host structure with the inclusion of Fe and/or Co. Overall, the dPDF analysis provides the needed expanded insights into the structure of atomically dispersed catalysts beyond the local coordination of the metal atoms to help better understand structure/function relationships for these materials.

To further confirm structural findings, DFT calculations were then conducted. The optimized structures of the single-atomic metals on NC substrates are shown in Fig. 3c-f. It can be observed in Fig. 3c and Fig. 3d, the center single Fe (Co) atom is coordinated to the 4 nearest N atoms, and the average Fe-N (Co-N) distance is measured to be 1.89 Å (1.87 Å). These values are consistent with the fitting of the EXAFS data (2.00 Å for Fe-N and 1.93 Å for the Co-N), suggesting the suitability of the models built here. We further evaluated the structures of Co-Fe dimer on the NC substrate. For the highly ordered structure, the average Fe-N, Co-N, and Co-Fe distances were computed to be 1.95 Å, 1.92 Å, and 2.17 Å, respectively, see Fig. 3e. For the slightly distorted structure shown in Fig. 3f, the above values are predicted to be 1.93 Å, 1.93 Å, and 2.12 Å, respectively. These values are consistent with experiments from EXAFS and PDF measurements (1.94 Å for Fe-N, 1.85 Å for Co-N, and 2.07 Å for Co-Fe). To further test the validity of the DFT simulations, XANES calculations we performed using the DFT structures as input (see Supporting Information for more details). The calculated XANES spectra (Fig. S12) are in good agreement with

the experimental XANES reported in Fig. 2 and are consistent with previously reported materials.^{16, 47}

Electrocatalytic ORR Activity and Zinc Air Battery Test

The ORR performances of the catalysts were evaluated using the rotating ring-disk electrode (RRDE) in O₂-saturated 0.1 M KOH solution. It is well known that the carbonization temperature also has a great influence on the catalytic performance. The catalysts were pyrolyzed at 800 °C (CoFe-NC-800), 900 °C (CoFe-NC-900) and 1000 °C (CoFe-NC-1000), and the ORR performance are illustrated in Fig. S1. It can be noted that, CoFe-NC-900 possessed the most outstanding half wave potential of 0.94 V compared with CoFe-NC-800 of 0.87 V and CoFe-NC-1000 of 0.88 V. Based on the above results, the calcination temperature of 900 °C were chosen as the optimal temperature for preparing the CoFe-NC catalyst. To achieve the optimal performance of atomically dispersed catalyst with Co, Fe dual sites, we investigated the effects of the weight percentage of Co, Fe on the catalytic activity. By set the Co-to-Fe molar ratio as 1: 1, the half wave potential of the catalysts first increased then decreased with the increasing of the metal amount (Fig. S2). When the weight percentage of Co, Fe increased from 25%, 30%, to 35%, the half-wave potential gradually increased from 0.78 V, 0.82 V, to 0.94 V, indicating that the effective active sites were gradually enriched, but continuously increasing the weight percentage to 40% and 45%, the half wave potential attenuated to 0.86 V and 0.82 V, respectively, indicating that excessive metal amount might led to aggregation of single atom sites. Subsequently, we further

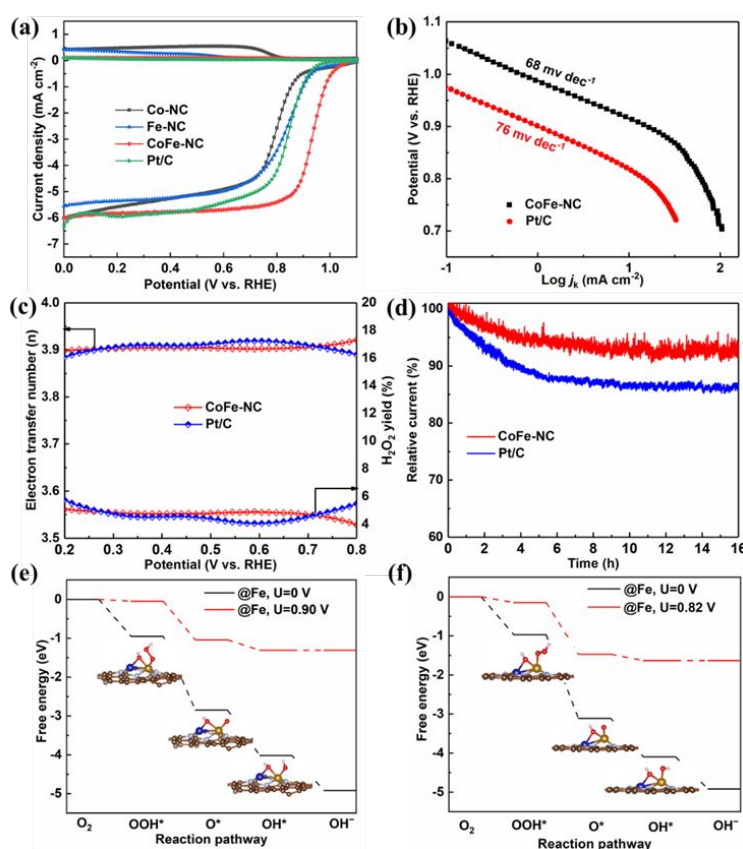


Fig. 4. The ORR performance of the different catalysts. (a) The LSV curves of Co-NC, Fe-NC, CoFe-NC, and Pt/C measured in O₂-saturated 0.1 M KOH with a rotation rate of 1600 rpm; (b) Tafel plots of CoFe-NC and Pt/C; (c) The H₂O₂ yield and electron transfer numbers of CoFe-NC and Pt/C; (d) The *i*-*t* curves of CoFe-NC and Pt/C at 0.85 V with 900 rpm. Free energy diagram of ORR at each elementary step on the (e) Fe site of Co-Fe dual atoms with adsorbed OH on the slightly disordered NC substrate and (f) Fe site of Co-Fe dual atoms with adsorbed OH on the ordered NC substrate. The optimized structures are also shown as insets in the figures.

explored the relationship between the Co-to-Fe molar ratio and its electrocatalytic activity. As shown in **Fig. S3**, the catalytic performance of the samples first enhanced then declined with the decrease of the Co content, and the best performance can be obtained when the molar ratio of Co-to-Fe is 1: 1 (CoFe-NC, $E_{1/2} = 0.94$ V). It suggests that the catalyst probably has the most appropriate adsorption energy for oxygen molecules when the ratio of Co-to-Fe is 1: 1.

The polarization curves of Co-NC, Fe-NC, CoFe-NC, and Pt/C are shown in **Fig. 4a**. The half wave potential of CoFe-NC (0.94 V) is higher than that of Co-NC (0.80 V) and Fe-NC (0.83 V), and more intriguingly, is 90 mV higher than Pt/C (0.85 V). The ORR performance of CoFe-NC was further evaluated and compared with Pt/C. **Fig. S13** shows the RDE voltammograms recorded with different rotation rates for CoFe-NC and Pt/C. Note that, the current densities increased with the increasing of the rotation rate for both samples, where in the mixed kinetics/diffusion controlled region, excellent linearities with rather consistent slopes were acquired in the Koutecky-Levich (K-L) plots for both samples. These results indicate a first reaction kinetics for ORR with respect to the oxygen concentration in the solution. **Fig. 4b** shows the Tafel plots for CoFe-NC and Pt/C, where CoFe-NC exhibited a smaller Tafel slope value of 68 mV dec⁻¹ than Pt/C (76 mV dec⁻¹) in alkaline solution, implying that CoFe-NC possesses a faster reaction kinetics. In addition, the electron transfer number and yield of H₂O₂ for both CoFe-NC and Pt/C in the potential range of 0.2-0.8 V were calculated by **Equations 1** and **2**. As illustrated in **Fig. 4c**, CoFe-NC had the electron transfer number of 3.90-3.92, comparable to Pt/C (3.88-3.92). In addition, the H₂O₂ yield of CoFe-NC (3.81%-3.92%) is slightly lower than that of Pt/C (4.22%-9.23%), suggesting improved ORR selectivity in alkaline solution. Finally, the durability of CoFe-NC was evaluated and compared with Pt/C by amperometric *i*-t curves at 0.85 V with a rotation speed of 900 rpm. As shown in **Fig. 4d**, after 16 hours of continuous operation, CoFe-NC maintained 92% of the initial current, much higher than that of Pt/C (86%), indicating an improved long-term stability of CoFe-NC over this period of time.

Moreover, the ORR performance of CoFe-NC was also assessed and compared with Pt/C in 0.1 M HClO₄. **Fig. S14a** shows the polarization curves, where CoFe-NC possessed a half wave potential of 0.80 V, higher than that of Co-NC and Fe-NC, but slightly inferior to the Pt/C catalyst (0.85 V). The 50 mV difference is reasonable, as Pt/C possessed incomparable performance in acid media. **Fig. S15** depicts the current density change with the change of rotation rate, with highly linear responses observed in the K-L plots for both samples, suggesting a first-order reaction kinetics for both samples. The subsequently extrapolated Tafel plots are presented in **Fig. S14b**, where CoFe-NC exhibited a slightly lower but comparable Tafel slope value with Pt/C, an indication of the comparable intrinsic catalytic behaviors. In addition, CoFe-NC also demonstrated close values of numbers of electron transferred and yields of H₂O₂ with Pt/C (**Fig. S14c**). Lastly, in the *i*-t test (**Fig. S14d**), CoFe-NC retained 88% of its initial current, superior to

that of Pt/C (76%). It shows that CoFe-NC has an improved long-term durability over Pt/C in acidic media as well.

It is worth noting that the ORR performance of CoFe-NC in alkaline media is markedly improved over recently reported M-N_x-C based atomically dispersed catalysts (see **Table S6**). We attribute the improved ORR performance in alkaline media to the well-defined atomically dispersed structure of CoFe-NC with Co, Fe dual sites enriched onto the surface of the carbon sphere. The uniform micropores in the carbon substrate are beneficial for the adsorption of Fe³⁺, Co²⁺ ions, which can increase the loading of the active sites (4.78 wt.% from ICP-AES). In addition, the large specific surface area of CoFe-NC (**Fig. 1d**, 830 m² g⁻¹) can not only enhance the accessibility of O₂ molecules, but also impart Co-Fe dual sites are homogeneously dispersed (the HAADF-STEM image in **Fig. 2a**), which improve the utilization of the active sites. The addition of NH₄Cl in the synthesis as an additional nitrogen source dramatically increased the content of pyridinic N (shown in **Fig. S5b**) in CoFe-NC, where pyridinic N can enhance the surface wettability, boost the onset potential and half-wave potential;⁴⁸ Finally and the most importantly, the unique coordination structure of the sample (N₃Co-FeN₃, shown in **Fig. S8**) can lead to charge redistribution of the neighboring atoms, resulting in a synergistic effect between the dual active sites (CoN₃ and FeN₃), which eventually promoted oxygen activation by weakening the O=O bond.^{24, 25}

To gain some insight into the mechanism, we first calculated the adsorption of a single O₂ molecule on substrates decorated with transition metals. The relaxed structures are shown in **Fig. S16**. The O₂ molecule preferentially adsorbs above the transition metals through a side-on mode. Upon chemisorption, the O=O bond elongates from 1.21 Å in an isolated gas state to 1.39 Å for the Fe SA, 1.35 Å for the Co SA, and 1.44 Å for the Co-Fe dimer. The adsorption free energies were calculated to be -0.50 eV for the Fe SA, and 0.29 eV for the Co SA, respectively. Significantly, the adsorption free energy for O₂ molecule on the Co-Fe sites was computed to be -1.02 eV and -1.70 eV for the ordered and disordered substrates, respectively. The more negative adsorption energies and the longer O=O bond suggest an increased interaction between the O₂ molecule and the Co-Fe dimer sites, implying an improved ORR performance consistent with the findings of Shi et al.⁴⁹

The plots of charge density difference between the adsorbed O₂ molecule and the substrates are shown in **Fig. S17**, where the accumulation of electrons between the metal and O suggests a formation of M-O σ bonds. From the Bader charge analysis (see **Table S3** for the values), one can observe a stronger electron loss for the Co-Fe dimer sites compared to SA Fe and SA Co. In agreement with the correlation between a less positive metal center and enhanced ORR activity by suggested Li et al.,⁵⁰ the Co-Fe dimer sites on the slightly disordered NC are expected to display a better ORR performance compared to the other systems studied.

The ORR mechanism for the Co-Fe dimer was then investigated by following Nørskov's work.⁵¹ As shown in **Fig. S18a**, each reaction step for the Co-Fe sites on the highly ordered NC is exothermic. However, the free energy of the OH* formation reaction from O* is low, suggesting that it is rate-limiting. The

reaction free energy for the Co-Fe dimer sites on the slightly disordered NC is shown in **Fig. S18b**, where the OH* removal step is endothermic. As suggested by Li et al.,²⁵ OH* is anchored at the Co-Fe bridge during ORR. We will denote the OH* adsorbed on the Co-Fe dimer sites as CoFe-OH, see **Fig. S18b** inset. The ORR free energy diagram at the Fe site of CoFe-OH on disordered NC is shown in **Fig. 4e**. Each ORR step is exothermic, and the limiting potential (the maximum external potential at which the ORR processes are still exothermic) is predicted to be 0.90 V, a value even higher than that of Pt (0.79 V).²⁵ The free energy diagram at the Co site is displayed in **Fig. S19a**, showing a limit potential of only 0.58 V. After comparing the total energy of each intermediate adsorbed on the substrate, we can conclude that the ORR steps are likely to take place at the Fe site because of the lower computed energies. As a comparison, we also explored the ORR mechanism at the Fe site of CoFe-OH on highly ordered NC and show the results in **Fig. 4f**. It is noticed that the limit potential is 0.82 V, lower than that of the disordered one. We must also observe that the limiting potential for the Co-Fe dimer sites on highly ordered and slightly disordered NC is higher than those of SA Fe (0.54 V) and SA Co (0.81 V) (shown in **Fig. S19b** and **c**), suggesting synergy between the Fe and Co in the Co-Fe dimer. Furthermore, the disorder of the NC substrate appears to make additional contributions to the ORR as an identical dimer on a slightly disordered substrate shows better activity compared to that on the highly ordered substrate.

The interaction between an adsorbed O₂ molecule and the transition metal atoms can be better understood using the molecular orbital theory, as shown in **Fig. S20**. The calculations show that strong π bond (in-phase combination of d_{xz} orbital of Fe or Co and one π^* orbital of O₂) and a weak δ bond (in-phase combination of d_{xy} orbital of Fe or Co and the other π^* orbital of O₂)⁵² form in the structure with only one single metal atom catalyst, see **Fig. S20a**. However, in the presence of the Co-Fe dimer, two strong π bonds are formed. These two π bonds consist of in-phase and the out-of-phase combinations of d_{z2} orbitals of Fe and Co interacting with the π^* orbital of O₂, see **Fig. S20b**. The distortion of the O=O bond matches the in-phase combination of d_{z2} orbital to form the π bond. Detailed visualization of the orbital interactions using the principal interacting spin orbitals (PISO)⁵³ is shown in **Fig. S21-S26**. As suggested by Lin et al.,⁵³ the sum of all PISO-based bond indices can be regarded as the bond order, which can be further used to compare the bonding strength of the adsorbate O₂ with different substrates. As a result, the indices were calculated to be 2.15, 1.91, and 2.41 for the SA Fe, SA Co, and the Co-Fe dimer, respectively, suggesting its strong interaction with the substrate. These values are also consistent with the above analysis, supporting the conclusion that Co-Fe dimer has the best ORR performance among the materials studied.

The excellent ORR performance of the CoFe-NC catalyst inspired us to explore its practical application in zinc-air batteries (ZABs). A primary ZAB was constructed by using zinc foil as the anode, CoFe-NC as air cathode and 0.2 M Zn(OAc)₂ in 6 M KOH as electrolyte. The commercial Pt/C catalyst was employed to compare the discharge capability of the ZAB with CoFe-NC,

while for integrated charge and discharge test, a ZAB performance comparison was made between the CoFe-NC+IrO₂ catalyst and the Pt/C+IrO₂ catalyst. **Fig. 5a** presents the discharge polarization curves and power densities, where the CoFe-NC modified ZAB exhibited a power density of 115 mW cm⁻², much larger than the Pt/C decorated ZAB (85 mW cm⁻²). Meanwhile, as demonstrated in **Fig. 5b**, the specific capacity of the CoFe-NC modified ZAB is 791 mA h g⁻¹, also higher than that of the Pt/C decorated ZAB (707 mA h g⁻¹). Subsequently, the long-term stability of the CoFe-NC+IrO₂ and Pt/C+IrO₂ air cathodes were evaluated at 10 mA cm⁻² with each cycle of 10 min (**Fig. 5c**). For the CoFe-NC+IrO₂ based battery, the discharge voltage remained almost constant at 1.2 V for about 80 h, and the charge voltage kept as 2.0 V for about 70 h but gradually increased to 2.2 V at 80 h. In comparison, both the discharge and charge voltages can only remain stable for 30 h and increased drastically at 40 h for the Pt/C+IrO₂ based battery. Lastly, two ZAB cells with CoFe-NC air cathode connected in series can light up the blue LED lamps (voltage of ~3.0 V, **Fig. 5d**), showing this battery is a promising power device for practical application. Moreover, the performance of the CoFe-NC based battery has exceeded or at least is comparable with the recently documented M-N-C atomically dispersed catalysts, and the detailed comparison regarding the power density, specific capacity and charge-discharge stability are summarized in Table S7. The above results fully validate that CoFe-NC could be a promising alternative for the Pt/C catalyst in practical ZAB implementation as well.

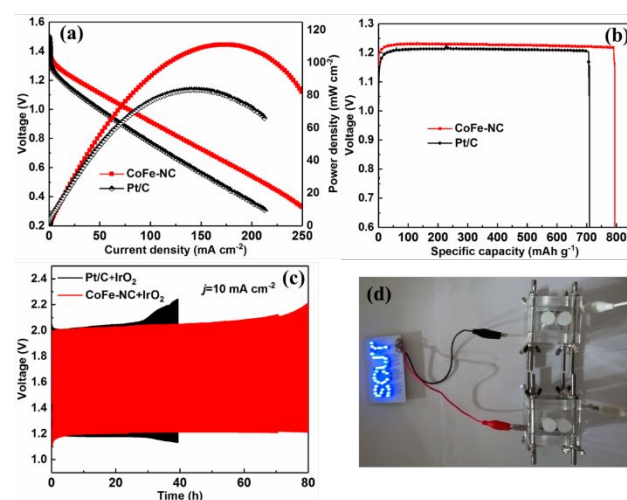


Fig. 5. (a) The discharge polarization curves and their corresponding power density curves with CoFe-NC and Pt/C as air cathode; (b) The discharge specific capacities of the CoFe-NC and Pt/C air-cathodes at 10 mA cm⁻²; (c) The charge-discharge plots of the ZABs based on the CoFe-NC+IrO₂ air cathode and Pt/C+IrO₂ air cathode; (d) The photograph of a blue LED (V ≈ 3.0 V) powered by two liquid Zn-air batteries with CoFe-NC air cathode connected in series.

Conclusion

In summary, we developed a facile strategy to prepare atomically dispersed catalyst with Co, Fe dual sites enriched onto the surface of microporous carbon. Such strategy can impart a maximal exposure of Co, Fe dual sites and lead to a

high utilization of active sites. As a result, the as-prepared CoFe-NC catalyst exhibited a superior ORR performance to the Pt/C catalyst in alkaline media. As air cathode, CoFe-NC also outperformed Pt/C in the primary zinc air battery test. More importantly, XAS measurements show that the bimetallic atoms regulate each other's electronic structure and directly affect the coordination environment, while the PDF analysis demonstrate that the metal atoms can tune the lattice structure of the NC, likely modifying its electronic properties. DFT calculations reveal that, the atomic Co-Fe dimers lie on the slightly disordered NC rather a highly ordered substrate, which agree with our synchrotron structural analysis, and indicate that such configurations can provide the appropriate adsorption free energies of the oxygenated species, hence promoting the process of ORR and the primary zinc-air battery performance. This study not only provides a new facile strategy for preparing atomically dispersed dual metal sites catalyst, but also clearly elucidates the metal-substrate interaction and unravels its impact on the catalytic performance. We envision that the findings here will be beneficial for the future rational design of atomically dispersed catalysts toward ORR and beyond.

Author Contributions

Kai Wang: Conceptualization, Methodology, Investigation, Formal analysis, Writing-original draft. Jiapeng Liu: Methodology, Theoretical calculation, Writing-original draft. Zhenghua Tang: Conceptualization, Resources, Writing-review & editing, Funding support. Ligui Li: Investigation. Zheng Wang: Investigation. Muhammad Zubair: Investigation. Francesco Ciucci: Resources, Theoretical calculation, Writing-review & editing, Funding support. Lars Thomsen: Investigation, Resources. Joshua Wright: Investigation. Resources. Nicholas M. Bedford: Investigation, Resources, Writing-review & editing, Funding support.

Conflicts of interest

The authors declare that they have no known competing financial interests or personal relationships that could have appeared to influence the work reported in this paper.

Acknowledgements

This study is supported from the Research Fund Program of Key Laboratory of Fuel Cell Technology of Guangdong Province. Z. T. thanks the financial support from Guangzhou Science and Technology Plan Projects (No. 201804010323), and Guangdong Natural Science Funds for Distinguished Young Scholars (No. 2015A030306006). F. C. gratefully acknowledges the support of the Hong Kong Innovation and Technology Fund (No. ITS/292/18FP), Research Grants Council of Hong Kong (16207615, 16227016, and 16204517), and the Guangzhou Science and Technology Program (No. 201807010074). This research used the 10-BM and 11-ID-B beamlines of the Advanced Photon Source, a U.S. Department of Energy (DOE)

Office of Science User Facility operated for the DOE Office of Science by Argonne National Laboratory under Contract No. DE-AC02-06CH11357. 10-BM is further supported by the DOE and the Materials Research Collaborative Access Team member institutions. M.Z. acknowledges scholarship support from the Scientia PhD Scholarships program at UNSW. We would like to thank Leighanne Gallington for assistance with experiments at 11-ID-B. NEXAFS measurements were performed on the SXR beamline at the Australian Synchrotron, part of the Australian Nuclear Science and Technology Organisation (ANSTO), and funded by the Australian Government. N.M.B acknowledges partial financial support from the Faculty of Engineering at UNSW and travel funding provided by the International Synchrotron Access Program managed by the Australian Synchrotron.

References

1. M. Lefevre, E. Proietti, F. Jaouen and J. Dodelet, *Science*, 2009, **324**, 71-74.
2. J. Suntivich, H. A. Gasteiger, N. Yabuuchi, H. Nakanishi, J. B. Goodenough and Y. Shaoorn, *Nat. Chem.*, 2011, **3**, 546-550.
3. C. Tang and Q. Zhang, *Adv. Mater.*, 2017, **29**, 1604103.
4. C. Wang, N. M. Markovic and V. R. Stamenkovic, *ACS Catal.*, 2012, **2**, 891-898.
5. L. Dai, Y. Xue, L. Qu, H.-J. Choi and J.-B. Baek, *Chem. Rev.*, 2015, **115**, 4823-4892.
6. X. X. Wang, M. T. Swihart and G. Wu, *Nat. Catal.*, 2019, **2**, 578-589.
7. Y. Chen, S. Ji, C. Chen, Q. Peng, D. Wang and Y. Li, *Joule*, 2018, **2**, 1242-1264.
8. Y. He, S. Hwang, D. A. Cullen, M. A. Uddin, L. Langhorst, B. Li, S. Karakalos, A. J. Kropf, E. C. Wegener, J. Sokolowski, M. Chen, D. Myers, D. Su, K. L. More, G. Wang, S. Litser and G. Wu, *Energy Environ. Sci.*, 2019, **12**, 250-260.
9. G. Wu, K. L. More, C. M. Johnston and P. Zelenay, *Science*, 2011, **332**, 443-447.
10. Y. Chen, S. Ji, Y. Wang, J. Dong, W. Chen, Z. Li, R. Shen, L. Zheng, Z. Zhuang, D. Wang and Y. Li, *Angew. Chem., Int. Ed.*, 2017, **56**, 6937-6941.
11. H.-W. Liang, W. Wei, Z.-S. Wu, X. Feng and K. Müllen, *J. Am. Chem. Soc.*, 2013, **135**, 16002-16005.
12. N. R. Sahraie, U. I. Kramm, J. Steinberg, Y. Zhang, A. Thomas, T. Reier, J.-P. Paraknowitsch and P. Strasser, *Nat. Commun.*, 2015, **6**, 8618.
13. X. Wan, X. Liu, Y. Li, R. Yu, L. Zheng, W. Yan, H. Wang, M. Xu and J. Shui, *Nat. Catal.*, 2019, **2**, 259-268.
14. A. Zitolo, N. Ranjbar-Sahraie, T. Mineva, J. Li, Q. Jia, S. Stamatini, G. F. Harrington, S. M. Lyth, P. Krtil, S. Mukerjee, E. Fonda and F. Jaouen, *Nat. Commun.*, 2017, **8**, 957.
15. J. Li, M. Chen, D. A. Cullen, S. Hwang, M. Wang, B. Li, K. Liu, S. Karakalos, M. Lucero, H. Zhang, C. Lei, H. Xu, G. E. Sterbinsky, Z. Feng, D. Su, K. L. More, G. Wang, Z. Wang and G. Wu, *Nat. Catal.*, 2018, **1**, 935-945.
16. H. Fei, J. Dong, Y. Feng, C. S. Allen, C. Wan, B. Voloskiy, M. Li, Z. Zhao, Y. Wang, H. Sun, P. An, W. Chen, Z. Guo, C. Lee, D. Chen, I. Shakir, M. Liu, T. Hu, Y. Li, A. I. Kirkland, X. Duan and Y. Huang, *Nat. Catal.*, 2018, **1**, 63-72.

17. J. Li, S. Chen, N. Yang, M. Deng, S. Ibraheem, J. Deng, J. Li, L. Li and Z. Wei, *Angew. Chem. Int. Ed.*, 2019, **58**, 7035-7039.
18. F. Li, G.-F. Han, H.-J. Noh, S.-J. Kim, Y. Lu, H. Y. Jeong, Z. Fu and J.-B. Baek, *Energy Environ. Sci.*, 2018, **11**, 2263-2269.
19. M. Xiao, J. Zhu, G. Li, N. Li, S. Li, Z. P. Cano, L. Ma, P. Cui, P. Xu, G. Jiang, H. Jin, S. Wang, T. Wu, J. Lu, A. Yu, D. Su and Z. Chen, *Angew. Chem., Int. Ed.*, 2019, **58**, 9640-9645.
20. E. Luo, H. Zhang, X. Wang, L. Gao, L. Gong, T. Zhao, Z. Jin, J. Ge, Z. Jiang, C. Liu and W. Xing, *Angew. Chem., Int. Ed.*, 2019, **58**, 12469-12475.
21. M. Xiao, L. Gao, Y. Wang, X. Wang, J. Zhu, Z. Jin, C. Liu, H. Chen, G. Li, J. Ge, Q. He, Z. Wu, Z. Chen and W. Xing, *J. Am. Chem. Soc.*, 2019, **141**, 19800-19806.
22. H. Sun, M. Wang, S. Zhang, S. Liu, X. Shen, T. Qian, X. Niu, J. Xiong and C. Yan, *Adv. Funct. Mater.*, 2021, **31**, 2006533.
23. J. Wang, L. Gan, W. Zhang, Y. Peng, H. Yu, Q. Yan, X. Xia and X. Wang, *Sci. Adv.*, 2018, **4**, eaap7970.
24. J. Wang, Z. Huang, W. Liu, C. Chang, H. Tang, Z. Li, W. Chen, C. Jia, T. Yao, S. Wei, Y. Wu and Y. Li, *J. Am. Chem. Soc.*, 2017, **139**, 17281-17284.
25. J. Wang, W. Liu, G. Luo, Z. Li, C. Zhao, H. Zhang, M. Zhu, Q. Xu, X. Wang, C. Zhao, Y. Qu, Z. Yang, T. Yao, Y. Li, Y. Lin, Y. Wu and Y. Li, *Energy Environ. Sci.*, 2018, **11**, 3375-3379.
26. M. Xiao, Y. Chen, J. Zhu, H. Zhang, X. Zhao, L. Gao, X. Wang, J. Zhao, J. Ge, Z. Jiang, S. Chen, C. Liu and W. Xing, *J. Am. Chem. Soc.*, 2019, **141**, 17763-17770.
27. Z. Lu, B. Wang, Y. Hu, W. Liu, Y. Zhao, R. Yang, Z. Li, J. Luo, B. Chi, Z. Jiang, M. Li, S. Mu, S. Liao, J. Zhang and X. Sun, *Angew. Chem., Int. Ed.*, 2019, **58**, 2622-2626.
28. G. Yang, J. Zhu, P. Yuan, Y. Hu, G. Qu, B.-A. Lu, X. Xue, H. Yin, W. Cheng, J. Cheng, W. Xu, J. Li, J. Hu, S. Mu and J.-N. Zhang, *Nat. Commun.*, 2021, **12**, 1734.
29. J. Wang, H. Liu, J. Diao, X. Gu, H. Wang, J. Rong, B. Zong and D. S. Su, *J. Mater. Chem. A*, 2015, **3**, 2305-2313.
30. Y. Fang, D. Gu, Y. Zou, Z. Wu, F. Li, R. Che, Y. Deng, B. Tu and D. Zhao, *Angew. Chem. Int. Ed.*, 2010, **49**, 7987-7991.
31. Y. He, S. Hwang, D. A. Cullen, M. A. Uddin, L. Langhorst, B. Li, S. Karakalos, A. J. Kropf, E. C. Wegener, J. Sokolowski, M. Chen, D. Myers, D. Su, K. L. More, G. Wang, S. Litster and G. Wu, *Energy Environ. Sci.*, 2019, **12**, 250-260.
32. J. Woo, Y. J. Sa, J. H. Kim, H.-W. Lee, C. Pak and S. H. Joo, *ChemElectroChem*, 2018, **5**, 1928-1936.
33. X. Fu, N. Li, B. Ren, G. Jiang, Y. Liu, F. M. Hassan, D. Su, J. Zhu, L. Yang, Z. Bai, Z. P. Cano, A. Yu and Z. Chen, *Adv. Energy Mater.*, 2019, **9**, 1803737.
34. L.-S. Zhang, X.-Q. Liang, W.-G. Song and Z.-Y. Wu, *Phys. Chem. Chem. Phys.*, 2010, **12**, 12055-12059.
35. K. G. Latham, W. M. Dose, J. A. Allen and S. W. Donne, *Carbon*, 2018, **128**, 179-190.
36. X. Wang, W. Chen, L. Zhang, T. Yao, W. Liu, Y. Lin, H. Ju, J. Dong, L. Zheng, W. Yan, X. Zheng, Z. Li, X. Wang, J. Yang, D. He, Y. Wang, Z. Deng, Y. Wu and Y. Li, *J. Am. Chem. Soc.*, 2017, **139**, 9419-9422.
37. G. R. S. Iyer and P. D. Maguire, *J. Mater. Chem.*, 2011, **21**, 16162-16169.
38. J. Yang, Z. Qiu, C. Zhao, W. Wei, W. Chen, Z. Li, Y. Qu, J. Dong, J. Luo, Z. Li and Y. Wu, *Angew. Chem., Int. Ed.*, 2018, **57**, 14095-14100.
39. L. Bai, C.-S. Hsu, D. T. L. Alexander, H. M. Chen and X. Hu, *J. Am. Chem. Soc.*, 2019, **141**, 14190-14199.
40. Z. Zhang, J. Sun, F. Wang and L. Dai, *Angew. Chem. Int. Ed.*, 2018, **57**, 9038-9043.
41. L. Tao, M. Qiao, R. Jin, Y. Li, Z. Xiao, Y. Wang, N. Zhang, C. Xie, Q. He, D. Jiang, G. Yu, Y. Li and S. Wang, *Angew. Chem., Int. Ed.*, 2019, **58**, 1019-1024.
42. J. Li, L. Jiao, E. Wegener, L. L. Richard, E. Liu, A. Zitolo, M. T. Sougrati, S. Mukerjee, Z. Zhao, Y. Huang, F. Yang, S. Zhong, H. Xu, A. J. Kropf, F. Jaouen, D. J. Myers and Q. Jia, *J. Am. Chem. Soc.*, 2020, **142**, 1417-1423.
43. M. Qiao, Y. Wang, Q. Wang, G. Hu, X. Mamat, S. Zhang and S. Wang, *Angew. Chem., Int. Ed.*, 2020, **59**, 2688-2694.
44. N. M. Bedford, H. Ramezani-Dakhel, J. M. Slocik, B. D. Briggs, Y. Ren, A. I. Frenkel, V. Petkov, H. Heinz, R. R. Naik and M. R. Knecht, *ACS Nano*, 2015, **9**, 5082-5092.
45. V. Petkov, *Mater. Today*, 2008, **11**, 28-38.
46. K. W. Chapman, P. J. Chupas and C. J. Kepert, *J. Am. Chem. Soc.*, 2005, **127**, 11232-11233.
47. X. Xie, C. He, B. Li, Y. He, D. A. Cullen, E. C. Wegener, A. J. Kropf, U. Martinez, Y. Cheng, M. H. Engelhard, M. E. Bowden, M. Song, T. Lemmon, X. S. Li, Z. Nie, J. Liu, D. J. Myers, P. Zelenay, G. Wang, G. Wu, V. Ramani and Y. Shao, *Nature Catalysis*, 2020, **3**, 1044-1054.
48. I. S. Amiinu, X. Liu, Z. Pu, W. Li, Q. Li, J. Zhang, H. Tang, H. Zhang and S. Mu, *Adv. Funct. Mater.*, 2018, **28**, 1704638.
49. Z. Shi and J. Zhang, *J. Phys. Chem. C*, 2007, **111**, 7084-7090.
50. Y. Chen, S. Ji, S. Zhao, W. Chen, J. Dong, W.-C. Cheong, R. Shen, X. Wen, L. Zheng, A. I. Rykov, S. Cai, H. Tang, Z. Zhuang, C. Chen, Q. Peng, D. Wang and Y. Li, *Nat. Commun.*, 2018, **9**, 5422.
51. J. K. Nørskov, J. Rossmeisl, A. Logadottir, L. Lindqvist, J. R. Kitchin, T. Bligaard and H. Jónsson, *J. Phys. Chem. B*, 2004, **108**, 17886-17892.
52. C. J. Cramer, W. B. Tolman, K. H. Theopold and A. L. Rheingold, *Prod. Nat. Acad. Sci. U. S. A.*, 2003, **100**, 3635.
53. J.-X. Zhang, F. K. Sheong and Z. Lin, *Chem. Eur. J.*, 2018, **24**, 9639-9650.